Remote Sensing of Environment 156 (2015) 129–142

Contents lists available at ScienceDirect

Remote Sensing of Environment

journal homepage: www.elsevier.com/locate/rse

Simulated impact of sensor field of view and distance on field measurements of bidirectional reflectance factors for row crops

Feng Zhao [a,*], Yuguang Li [a,b], Xu Dai [a], Wout Verhoef [c], Yiqing Guo [a], Hong Shang [a], Xingfa Gu [d], Yanbo Huang [e], Tao Yu [d], Jianxi Huang [f]

[a] School of Instrumentation Science and Opto-Electronics Engineering, Beijing University of Aeronautics and Astronautics, Beijing 100191, PR China
[b] College of Environmental Science and Forestry, State University of New York, 1 Forestry Dr, Syracuse, NY 13210, USA
[c] Faculty of Geo-information Science and Earth Observation (ITC), University of Twente, P.O. Box 217, 7500 AE Enschede, The Netherlands
[d] Institute of Remote Sensing and Digital Earth, Chinese Academy of Sciences, No. 20 Datun Road, Beijing 100101, PR China
[e] USDA-Agricultural Research Service, Crop Production Systems Research Unit, 141 Experiment Station Road, Stoneville, MS 38776, USA
[f] College of Information and Electrical Engineering, China Agricultural University, Beijing 100083, PR China

ARTICLE INFO

Article history:
Received 18 February 2014
Received in revised form 8 September 2014
Accepted 8 September 2014
Available online xxxx

Keywords:
Field measurements
Field of view
Bidirectional reflectance factor
Sensor footprint
Monte Carlo model
Weighted photon spread model (WPS)
Row crops

ABSTRACT

It is well established that a natural surface exhibits anisotropic reflectance properties that depend on the characteristics of the surface. Spectral measurements of the bidirectional reflectance factor (BRF) at ground level provide us a method to capture the directional characteristics of the observed surface. Various spectroradiometers with different field of views (FOVs) were used under different mounting conditions to measure crop reflectance. The impact and uncertainty of sensor FOV and distance from the target have rarely been considered. The issue can be compounded with the characteristic reflectance of heterogeneous row crops. Because of the difficulty of accurately obtaining field measurements of crop reflectance under natural environments, a method of computer simulation was proposed to study the impact of sensor FOV and distance on field measured BRFs. A Monte Carlo model was built to combine the photon spread method and the weight reduction concept to develop the weighted photon spread (WPS) model to simulate radiation transfer in architecturally realistic canopies. Comparisons of the Monte Carlo model with both field BRF measurements and the RAMI Online Model Checker (ROMC) showed good agreement. BRFs were then simulated for a range of sensor FOV and distance combinations and compared with the reference values (distance at infinity) for two typical row canopy scenes. Sensors with a finite FOV and distance from the target approximate the reflectance anisotropy and yield average values over FOV. Moreover, the perspective projection of the sensor causes a proportional distortion in the sensor FOV from the ideal directional observations. Though such factors inducing the measurement error exist, it was found that the BRF can be obtained with a tolerable bias on ground level with a proper combination of sensor FOV and distance, except for the hotspot direction and the directions around it. Recommendations for the choice of sensor FOV and distance are also made to reduce the bias from the real angular signatures in field BRF measurement for row crops.

1. Introduction

The earth's surface scatters radiation anisotropically, especially at the shorter wavelengths that characterize solar irradiance (Strahler, 1997; Walthall, Roujean, & Morisette, 2000). The anisotropy of surface scattering can be described by the bidirectional reflectance distribution function (BRDF) (Nicodemus, Richmond, Hsia, Ginsberg, & Limperis, 1977; Schaepman-Strub, Schaepman, Painter, Dangel, & Martonchik, 2006). Spectral measurements of the directional reflectance at ground level enable us to gain an understanding of the directional reflectance characteristics of the observed surface and energy–matter interactions (Milton, Schaepman, Anderson, Kneubühler, & Fox, 2009). Field measurement of the bidirectional reflectance factor (BRF) is further motivated by the development of surface reflectance models (Goel, 1988), applications of ground-based remote sensing sensors to aid farm management (El-Shikha, Waller, Hunsaker, Clarke, & Barnes, 2007), the normalization of multiple view angle remote sensing data acquired by satellite sensors with wide swaths (Zhao et al., 2013), vicarious calibration of airborne and space-borne remote sensing devices (Secker, Staenz, Gauthier, & Budkewitsch, 2001; Wang, Czapla-Myers, Lyapustin, Thome, & Dutton, 2011), and the validation of satellite-derived products, e.g. albedo (Huang et al., 2013).

Field measurements of the directional reflectance characteristics of vegetation have received widespread attention to better monitor

* Corresponding author. Tel.: +86-10-82315884.
E-mail address: zhaofeng@buaa.edu.cn (F. Zhao).

http://dx.doi.org/10.1016/j.rse.2014.09.011
0034-4257/

and measure the structure and state of ecosystems. The application of vegetation monitoring was almost concurrent with the early development of field spectroscopy (Milton et al., 2009). Because of the absence of consistent protocols and procedures for such measurements, spectroradiometers with various specifications were used under different mounting conditions to make directional reflectance measurements. Daughtry, Vanderbilt, and Pollara (1982) summarized these experiments for crops in the early 1980s, and showed that sensors with a field of view (FOV) from 15° to 28° were positioned from less than 2 m to 9 m or so above the ground. Since then, a series of field measurements of BRFs for crops and other short canopies were conducted with various types of sensor configurations (Table 1). We can see that sensors with different FOVs ranging from 3° to 25° were adopted and mounted on the support structures from less than 1 m to 6 m or so above the ground. The choice of sensor FOV and altitude (see notation a under Table 1) partly depends on the available instrument and mounting system in a given circumstance. However, measurement uncertainties can arise from the difference of spatial resolution and the variations of the target for the non-imaging spectroradiometer. The issue can be further compounded with the difficulty to accurately determine the actual measurement area of the sensor and the spatial non-uniform responsivity across the sensor FOV (Mac Arthur, MacLellan, & Malthus, 2012).

Few researchers have studied the impact of the choice of sensor FOV and distance to the target on the field measurement of BRFs of vegetation canopies. With the reflectance factors measured from nadir across the row direction, Daughtry et al. (1982) studied the variability of reflectance with sensor altitude for three different row crops and showed that the variance of reflectance factor measurements from nadir at low altitudes was attributable to row effects which disappeared at higher altitudes. In a previous study, we used the reverse ray tracing software POV-Ray (Persistence of Vision Ray-tracer, POV-team, 2009) to evaluate the influence of sensor FOV and distance on the field directional measurements for typical row canopies (Shang, Zhao, & Zhao, 2012). However, only the impact on four components' fractions (i.e. sunlit leaves, shaded leaves, sunlit soil and shaded soil) was studied, which should be more appropriate for the modeling of brightness temperature in the thermal infrared bands, as shown in the study by Ren et al. (2013).

This paper investigates how different sensor FOVs and distances affect the field measurements of BRFs for row canopies. Because of the difficulty to conduct the repeatable experiments under controlled conditions as in the laboratory, a Monte Carlo model to study the impact was developed and briefly described in Section 2. The evaluation of the model with field BRF measurements is provided. More comparison results with other state-of-the-art 3-D Monte Carlo models via the RAMI Online Model Checker (ROMC) (Widlowski et al., 2008) are in the companioning Supplement Data. In Section 4 the application of the model to study the impact of sensor FOV–distance combinations

Table 1
Examples of sensor FOV and altitude.

Investigator	Surface type	Canopy height (cm)	LAI (or %cover)	Sensor altitude above the ground (cm)[a]	Sensor FOV (°)
Kimes (1983)	Corn	33	0.65 (25%)	150	12
	Lawn	14	9.9 (97%)	150	
	Soybeans	77	4.6 (90%)	150	
	Orchard grass	22	1.1 (50%)	350	
Kimes et al. (1985)	Plowed field	NA	NA	200	12
	Annual grassland	3	<5%		
	Steppe grass	38	18%		
	Hard wheat	46	14%		
	Salt plain	9	20%		
	Irrigated wheat	76	70%		
Deering and Eck (1987)	Uniform grass	16	1.16 (90%)	606[b]	15
	Tufted grass	14	1.81 (79%)		
	Soya bean	85	5.68 (98%)		
Pinter, Jackson, and Moran (1990)	Cotton	31	0.42	160	15
	Cotton	21	0.18		
	Cotton	34	0.51		
	Wet wheat	97	4.86		
	Dry wheat	96	3.87		
	Furrowed soil	–	–		
Ranson, Irons, and Daughtry (1991)	Bluegrass sod	5	NA	200	15
	Bare soil	–	–		
Deering, Eck, and Grier (1992)	Shinnery oak	43.1	0.7 (60.2%)	606[b]	15
Eck and Deering (1992)	Steppe grassland	NA	3.59	500	15
			4.06		
Sandmeier and Itten (1999)	Grass lawn	3–3.5	NA	200	3
Vierling, Deering, and Eck (1997)	Wet sedge tundra	NA	<2	400	15
	Tussock tundra			NA	18
Abdou et al. (2001)	Dry lake surface	–	–	200	5
Giardino and Brivio (2003)	Colza field	NA	NA	120	25
	Herbaceous species	NA	NA	110	25
	Grass	NA	NA	110	8
	Snow	–	–	110	8
Strub, Schaepman, Knyazikhin, and Itten (2003)	Alfalfa	50	3–5.5	198.6[c]	3
Gamon, Cheng, Claudio, MacKinney, and Sims (2006)	Shrub	NA	NA	< 500	20
Gianelle and Guastella (2007)	Forbs grasses and legumes	NA	NA	150	10
Anderson et al. (2013)	Meadow	NA	3.41	23.6	21–25
Buchhorn, Petereit, and Heim (2013)	Moist non-acidic tundra	2–35	NA	200	8.5

[a] Researchers use sensor 'altitude', 'height', and 'distance' differently. In this paper, we also used them interchangeably. By 'altitude' or 'height', we mean the distance from the sensor to the ground at nadir. For 'distance', it is the distance from the sensor to the ground for any viewing angle. See Fig. 2 for an illustration.
[b] Values were estimated according to the circular area at nadir.
[c] Value was estimated according to the radius of the circular footprint at nadir.

on the field measurement of BRFs will be presented for two typical row canopy scenes. The paper ends with a conclusion and discussion.

2. Description of the model

Monte Carlo (MC) simulations offer a simple, flexible, yet rigorous approach to photon transport in a plant canopy, which can calculate multiple physical quantities, such as albedo, radiant energy distribution within the canopy, BRF, and fraction of vegetation absorbed photosynthetically active radiation (fAPAR) simultaneously (Govaerts & Verstraete, 1998; Ross & Marshak, 1988). In this paper we proposed a new MC model, so called the weighted photon spread (referred below as WPS) model. In WPS, a 3-D architecture of the canopy is generated to simulate the interaction of light with canopy elements. We divide the description of the model in its components.

2.1. Canopy generation

Vegetation components and soil in an architecturally realistic canopy are simulated by a number of polygons (triangular or 4-sided polygon), each with a specified set of reflectances and transmittances in different spectral bands. For the research targets of row crops in this study, a procedure as introduced in Zhao et al. (2010) was followed to generate typical row canopies, according to the designed row structure parameters, leaf area index (LAI) and leaf inclination distribution function (LIDF). Wood and stems are not included in the generated scene. The whole scene is enclosed in a cubical box, so as to emulate an infinite canopy by imposing that when a photon leaving the box from one side, it is supposed to enter the box from the opposite side. The scene is further divided into $M \times N \times K$ bounding boxes containing a certain number of polygons to improve the efficiency during ray intersection testing.

2.2. Simulation of photon propagation

In a radiative transport problem, the MC method consists of recording photon histories as they are scattered and absorbed. This process is repeated until the recorded albedo, and the reflectance factors approach stable values (e.g., within 1% variations). To achieve significantly faster simulations of BRF distributions, a variance reduction method known as 'photon spread' has been implemented by Thompson and Goel (1998), Widlowski, Lavergne, Pinty, Verstraete, and Gobron (2006), which resulted in the PS (photon spread) model and Rayspread model, respectively. The weight concept of the photon energy was used in the field of medical imaging to simulate laser–tissue interactions (Wang, Jacques, & Zheng, 1995) and in atmospheric radiative transfer modeling (Iwabuchi, 2006). Here we adapted this weight concept and combined it with the photon spread method to propose the WPS model. Except for the weight reduction approach, the concept of photon spreading in the architecturally realistic canopy is similar to the one of the PS model and the Rayspread model, so the elaboration on these aspects of the process was skipped.

Incident radiation can be simulated with a number of packets of photons from the solar direction and from the sky (diffuse radiation). The basic unit of packet is used instead of the photon because it is subject to split (to be discussed). The packet of photons is injected into the canopy from a randomly chosen (x, y) location on the upper cubical box with the directional cosines (μ_x, μ_y, μ_z) determined by the solar zenith angle (SZA, θ_s) and solar azimuth angle (SAA, φ_s). For the sky radiation, the isotropic distribution function is applied (Govaerts, 1996). When a photon hits a canopy element, a uniform random number between 0 and 1 is generated and compared with the probabilities of reflectance, transmittance and absorption events to determine the interaction type. With the spread method, if a reflection or transmission event occurs, the total radiation of the photon is allowed to spread and contribute to the detector with further interception tests. But an absorption event terminates photon movement and results in 'wasted' processing time in terms of simulating the BRF.

Instead of making the interaction type of the photon an all-or-nothing event (completely reflected, transmitted or absorbed), the weight concept (Wang et al., 1995; Iwabuchi, 2006) and the splitting approach are used each time when a photon packet strikes the canopy elements. We assume that many photons (a photon packet) follow a particular pathway simultaneously once injected into the scene. When the packet interacts with a canopy element, we reduce its weight by multiplying the previous weight with the probability of absorption of the element. In practice, the size of the packet in a spectral band with the wavelength λ is initially assigned a weight, $W_{0,\lambda}$, equal to unity. For reasons of clarity, we will omit the spectral dependence in the following explanation. After each intersection step with a canopy element, the photon packet is split into three parts (reflected, transmitted, and absorbed). The new weight (W_p) for the split photon packet is calculated as follows according to the weight of the incident photon packet (W_i) and the spectral properties of the element

$$W_p = \begin{cases} W_i \cdot \rho_s \quad \text{or} \quad W_i \cdot \rho_l & \text{if reflected by soil or leaf} \\ 0 \quad \text{or} \quad W_i \cdot \tau_l & \text{if transmitted by soil or leaf} \\ W_i \cdot (1-\rho_s) \quad \text{or} \quad W_i \cdot (1-\rho_l-\tau_l) & \text{if absorbed by soil or leaf} \end{cases} \tag{1}$$

where ρ_s and ρ_l are the soil reflectance and leaf hemispherical reflectance respectively, and τ_l is the leaf hemispherical transmittance. The tracing of the absorbed photon packet ends here, and the weight of its packet is accordingly recorded for the computation of fAPAR. The new reflected and transmitted photon packets in turn would be propagated and split. A recursive routine is designed to trace the photon packet until it escapes the scene or does not survive the Russian roulette (to be discussed).

Concurrently with the tracing of the photon packet, we spread the photon packet to the sensor. If it is intercepted by other elements, no contribution is recorded for the sensor. We then return to the interaction site and choose a direction of the reflected or transmitted packet using bi-Lambertian scattering law (Antyufeev & Marshak, 1990). If the packet spreads directly to the sensor without the interception by any element, we record its contribution to BRF. Similarly we return to the interaction site and trace the next packet as mentioned above. In conclusion, we obtain the distribution of radiation (radiation regime) in the canopy by tracing the photon packet, and compute the physical quantities using the spread method.

A technique called Russian roulette (Wang et al., 1995) is used in WPS to terminate a photon packet when the weight falls below a preset threshold W_{th} (e.g., $W_{th} = 0.0005$). This technique gives the photon packet one chance of m (e.g., $m = 10$) to survive with a new weight of mW. If the photon packet fails the roulette, we end the tracing of this packet by setting its weight to zero. This technique can be summarized as:

$$W = \begin{cases} mW & \text{if } x \le 1/m, \\ 0 & \text{if } x > 1/m \end{cases} \tag{2}$$

where x is a random number uniformly distributed in [0, 1]. This method terminates the photon packet in an unbiased manner while the total energy is conserved.

2.3. Measurement of physical quantities

During the MC simulation we accumulate the contributions of the scattered photon packet in the directions of the pre-defined sensors after every physical interaction. The counts of the photon packet scattered and elements from which it was scattered are also recorded to compute separate contributions of the different components of the scene, for instance the single and multiple scattering contributions

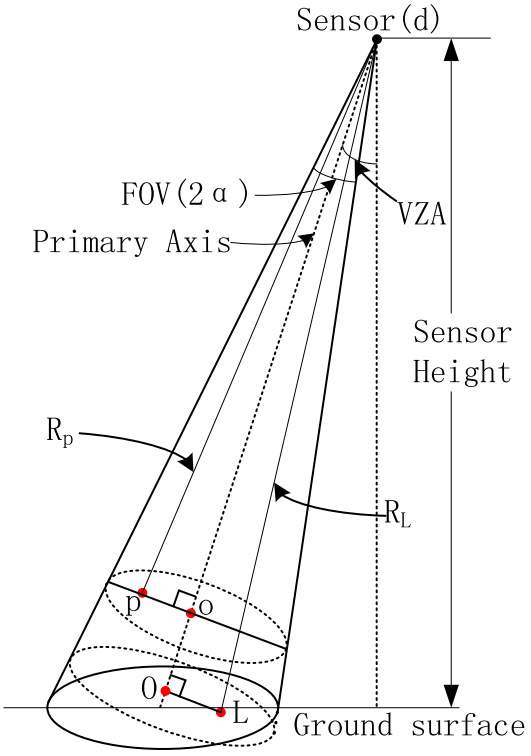

Fig. 1. Bidirectional reflectance factor measurement with a sensor of given height and instantaneous field of view (2α). See the text for detailed explanation of the quantities.

from leaf or soil to the total BRF. For a sensor d located at infinity, the resulting BRF value is obtained by:

$$\mathrm{BRF}\ (\lambda, \theta_o, \varphi_o) = \frac{\sum_{j=1}^{N_k} W_p |\mathbf{n}_d \cdot \mathbf{n}_e|}{N_{in} \cos\theta_o} \tag{3}$$

where N_{in} is the total number of photon packets emitted, and N_k is the number of the photon packets that has interacted with vegetative elements and spreads to the sensor without further interception; W_p is its weight as mentioned previously; vector $\mathbf{n}_d$ indicates the direction unit of the sensor with zenith and azimuth angles of θ_o and φ_o, respectively; and vector $\mathbf{n}_e$ represents the normal to the interacted canopy element (leaf or soil).

By Eq. (3), we suppose that an ideal detector with a particular viewing direction is located at infinity to collect the collimated radiation coming from an infinitely wide canopy, which is a true characterization of the intrinsic anisotropic properties of the target (Nicodemus et al., 1977). The resultant BRF will be assigned as the reference standards in the following.

Besides for the true directional simulation for a particular viewing direction, we can also calculate the amount of radiation reaching the sensor with a given FOV and height above the ground. This sensor-specific simulation (dependent on the sensor's FOV and height) allows for direct comparisons with actual measurement conditions. The BRF measured by the instrument with a solid angle of Ω is the ratio of reflected radiance into the sensor from the target to the radiance from an ideal diffuse reflector under the same irradiation conditions and observing geometry (Milton, 1987; Nicodemus et al., 1977). Suppose point p on a leaf with the normal of $\mathbf{n}_l$ is an interaction site as shown in Fig. 1. The photon packet with the weight W_p spreads from p to the sensor without interception. Suppose the initial radiant flux of the photon packet from the light source equals unity. Then the radiance contribution from point p in the projected circle of the primary axis to the sensor is given by

$$L_p(\lambda, \theta_o, \varphi_o) = \frac{\dfrac{W_p \left|\mathbf{n}_{pd} \cdot \mathbf{n}_l\right|}{\pi\left(R_p \left|\mathbf{n}_{pd} \cdot \mathbf{n}_{od}\right| \tan\alpha\right)^2}}{\Omega} \tag{4}$$

where R_p is the distance from p to the sensor, $\mathbf{n}_{pd}$ and $\mathbf{n}_{od}$ are the direction vectors (o is the center of the projected circle), and α is half of the FOV. Similarly the radiance contribution for the case of a point L in an ideal diffuse reflector on the ground surface with the normal of $\mathbf{n}_L$ is given by

$$L_L(\lambda, \theta_o, \varphi_o) = \frac{\dfrac{|\mathbf{n}_{Ld} \cdot \mathbf{n}_L|}{\pi(R_L |\mathbf{n}_{Ld} \cdot \mathbf{n}_{Od}| \tan\alpha)^2}}{\Omega} \tag{5}$$

where R_L is the distance from L to the sensor, and $\mathbf{n}_{Ld}$ and $\mathbf{n}_{Od}$ are the direction vectors (O is the center of the projected circle).

By the additions of all the radiance contributions of the canopy and of an ideal diffuse reflector enclosed in the FOV of the detector respectively, and the division of them, BRF is computed as

$$\mathrm{BRF}\ (\lambda, \theta_o, \varphi_o) = \frac{\sum_{j=1}^{N_k} \dfrac{W_p \left|\mathbf{n}_{pd} \cdot \mathbf{n}_l\right|}{\left(R_p \left|\mathbf{n}_{pd} \cdot \mathbf{n}_{od}\right|\right)^2}}{\sum_{i=1}^{N_{in}} \dfrac{|\mathbf{n}_{Ld} \cdot \mathbf{n}_L|}{(R_L |\mathbf{n}_{Ld} \cdot \mathbf{n}_{Od}|)^2}}. \tag{6}$$

The above derivations correspond to a perfect sensor, ignoring sensor noise, optical parameters, spectral and spatial point spread functions etc. However, those sensor-specific properties could be implemented once we establish the functions of the sensor. The simulation model has been coded using Visual C++ (Microsoft Visual Studio, 2012, Microsoft Inc., Redmond, WA). For the simulation of BRFs in 100 viewing directions for a canopy of about 2000 triangular polygons, the computer time without the weight method for a single band varies from a minimum of about 1 min for the red band to about 20 min for the near infrared (NIR) band to converge to a stable solution on a Windows-based personal computer (with 1.96 GB RAM and Pentium (R) Dual-Core CPU E5500 @ 2.8 GHz). For the same simulation, the time for WPS is about 20 min for the red band and 30 min for the NIR band. However, WPS can simulate BRFs in both bands with a single run. The increase of the number of bands will not significantly increase the computation time for WPS, because photons of different wavelengths travel along the same path through the ray intersection test, which is the most costly part of the MC simulation. So this weight and

Table 2
Measured canopy structural properties.

Date	Canopy height (cm)	Canopy width (cm)	Row spacing (cm)	LAI	ALA/standard deviation (deg.)
2004-4-1	7.8	5.9	15	1.3	29.6/25.0
2004-4-17	34.5	13.2	15	4.3	70.9/16.3

Table 3
Structural properties of the two row canopy scenes.

Scene	Row orientation	Canopy height (cm)	Canopy width (cm)	Row spacing (cm)	LAI	ALA/standard deviation (deg.)
Row-1	North–south	40	30	50	1.3	50.8/24. 4
Row-2	North–south	140	40	70	2.2	53.5/23.4

Table 4
Optical parameters of the two row canopy scenes.

Scene	SZA/SAA (deg.)	Ratio of direct solar radiation		ρ_l		ρ_s		τ_l	
		Red	NIR	Red	NIR	Red	NIR	Red	NIR
Row-1	15/210, 45/140	1	1	0.079	0.431	0. 163	0.209	0.036	0.53
Row-2	25/220, 46/105								

splitting combined approach is advantageous for multispectral, and especially hyperspectral simulations.

3. Material and methods

3.1. Data sets for model evaluation

Two data sets collected on April 1 (Day-1) and April 17 (Day-2), 2004 in Xiaotangshan located in Changping District, Beijing, China, were used to evaluate WPS. The experimental site mainly consisted of north–south row-planted winter wheat. Row spacing (distance between rows) of the mechanically sowed wheat canopy was 15 cm. Zhao et al. (2010) gave detailed information about these data sets and used them to validate their analytical BRDF model of row crops (referred below as Row). Here only the statistical structural parameters of the row canopies are provided, as listed in Table 2, where canopy height is mean height of plants, and canopy width is mean width of the plants within the row. Measured average leaf angle (ALA) and the standard deviation of the normal to the leaves were also provided. The ASD FieldSpec Pro spectroradiometer (ASD Inc., Boulder, CO., USA) with a 25° FOV fiber optic adapter was mounted on a goniometric instrument to measure canopy multi-angular radiation. The goniometer enables directional observations of the same target and keeps the distance from the spectrometer to the center of the target unchanged while moving over the target. The distance from the spectrometer to the center of the target was 160 cm. From the structural parameters and the pictures of the canopy taken by a digital camera, two scenes were generated to simulate BRFs by WPS under identical measurement conditions (e.g. sensor FOV and distance). The spectral and multi-angular measurements were carried out for VZA from −60° (forward direction) to 60° (backward direction) with a step of 5° in the following four viewing planes: the principal plane (PP, viewing azimuth angle aligned with solar azimuth angle), the cross plane (CP), the along row plane (AR, the plane along row direction), and the cross row plane (CR, the plane perpendicular to the row direction). SZA and SAA for Day-1 were (45°, 134°), (44°, 136°), (43°, 138°) and (42°, 139°) for PP, CP, AR, and CR, respectively. For Day-2 they were (39°, 132°), (38°, 134°), (37°, 136°) and (36°, 137°), respectively.

3.2. The design of the experiments to study FOV and distance impact

Two canopy scenes with north–south orientation (Row-1 and Row-2) were generated to simulate typical row crops in an intermediate growing stage, such as cotton, soybean and corn, upon which WPS was used to study FOV and distance impact on field BRF measurement. The structural properties of the scenes are summarized in Table 3. Leaves represented by isosceles triangles with adjustable sides and orientation were randomly distributed in the scenes. ALAs and their standard deviations in the scenes were also provided.

The spectral values of leaf and soil, information about sun angles and the ratios of direct radiation in two characteristic spectral bands of vegetation (red and NIR bands) are listed in Table 4. The four solar positions were chosen correspondingly to the local times from 10 h to 16 h in summer near Beijing (40°11′ N, 116°27′ E). The spatial and spectral point spread functions of the sensor were not considered because they are very sensor-specific and require comprehensive assessment (Mac Arthur et al., 2012). For simplicity, we only considered the direct solar light and ignored the diffuse skylight, which are not expected to significantly change the features of directional reflectance distributions of row canopies under clear sky conditions (Zhao et al., 2010).

The field protocols for BRF measurements are constrained by the devices, system configuration, data acquisition time, and infrastructural conditions for specific targets. Because most field instruments have replaceable optics that can modify the FOV (Walthall et al., 2000) and can be positioned at an adjustable height, we focus on the impact of sensor FOV and distance combinations on measured directional properties of the target. With reference to the frequently used spectro-radiometers for field experiment (e.g., ASD FieldSpec Pro, GER 3700 and OceanOptics HR), and the sensor distance mounted above the ground by previous researchers for typical crops (Table 1), we varied the sensor FOVs and distances as shown in Table 5 for the row canopies.

Reflectance factor computed by WPS with Eq. (3) was assigned as the reference value (RV) to evaluate the bias of the BRF measurements with the above sensor combinations to characterize the reflecting properties of the canopy (by Eq. 6). The calculations of BRFs were performed for VZA from −60° to 60° with a step of 5° in the four viewing planes: PP, CP, AR and CR. The mode that keeps the distance from the sensor to the target unchanged while looking at the same target continuously was adopted here for BRF simulations at ground level, as shown in Fig. 2. This mode, with the distances for off-nadir viewing angles from the sensor to the target equal to the sensor height above the ground at nadir (hereinafter termed as equal-distance mode) is widely used by the field and laboratory goniometer systems (Walthall et al., 2000).

The cross-section of the cone subtended from the sensor with the ground forms into circular (at nadir) or elliptical (off-nadir viewing angles) footprint, whose dimension depends on the sensor's FOV, distance to the target, and VZA. The expressions of the major and minor semiaxes

Table 5
Sensor FOV and distance settings for the two row canopy scenes.

Scene	Sensor FOV (deg.)	Sensor distance to target (cm)
Row-1	6, 8, 10, 15, 20, 25, 30	200, 300, 400, 500, 600, 700, 800
Row-2	6, 8, 10, 15, 20, 25, 30	300, 400, 500, 600, 700, 800

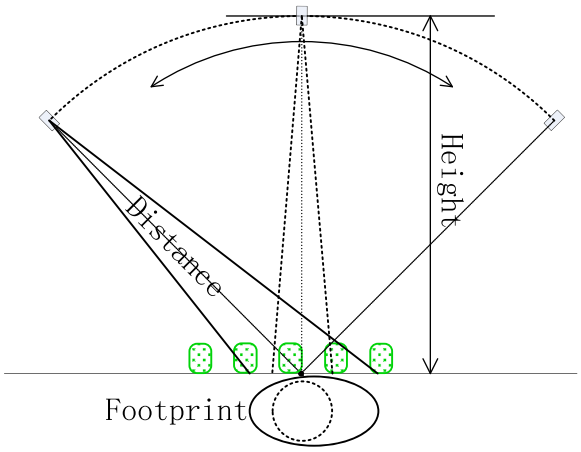

Fig. 2. Scheme of equal-distance multi-angle observations.

of the ellipse, a and b respectively, can be found in Deering and Leone (1986), and are provided here to facilitate the reading of the paper

$$a = \frac{H \tan\alpha\left(1 + \tan^2\theta_v\right)}{1-(\tan\alpha\tan\theta_v)^2}; \qquad b = \frac{H\tan\alpha}{\cos\theta_v\left[1-(\tan\alpha\tan\theta_v)^2\right]^{1/2}}. \quad (7)$$

where H is the sensor height above the ground at nadir. VZA (θ_v) should be less than ($\pi/2 - \alpha$) when applying the above equations. The area of the elliptic footprint (S) can be calculated by

$$S = \pi ab.$$

BRF measured with certain sensor's FOV and distance combination (R_O) and the corresponding reference value (R_{RV}) for the same canopy scene and sun-observing geometry were compared using the following statistics, the absolute percentage deviation (APD),

$$\mathrm{APD} = \frac{|R_{RV} - R_O|}{R_{RV}} 100\%. \quad (8)$$

To reduce the uncertainty associated with MC sampling, we averaged the results of multiple realizations (e.g. 5) under the same simulation conditions.

The image rendering software POV-Ray was employed to demonstrate what is contained in the sensor's FOV. POV-Ray uses a reverse ray-tracing method to render images, from which the quantities interested for remote sensing communities, such as four components' fractions (the visible sunlit leaves, shaded leaves, sunlit soil and shaded soil) and gap fractions of a canopy scene, can be derived. In our previous study, the effectiveness of POV-Ray's results of four components' fractions and gap fractions has been confirmed by systematic comparisons with the radiosity–graphics combined model (Wang et al., 2010). Based on the same canopy scene, we calibrated the setting of POV-Ray and WPS to ensure that the sensor (or camera for POV-Ray) is at the same location above the canopy and looks at the same point with the primary axis of the sensor pointing to the center of the scene on the ground. As a comparison with the images rendered for the ground level cameras as shown in Table 5, images were also rendered by POV-Ray for a sensor FOV–distance combination comparable to spaceborne remote sensing devices. By mimicking the compact high-resolution imaging spectrometer (CHRIS) on ESA's PROBA (Project for OnBoard Autonomy) platform (Cutter, 2004), we set the FOV to

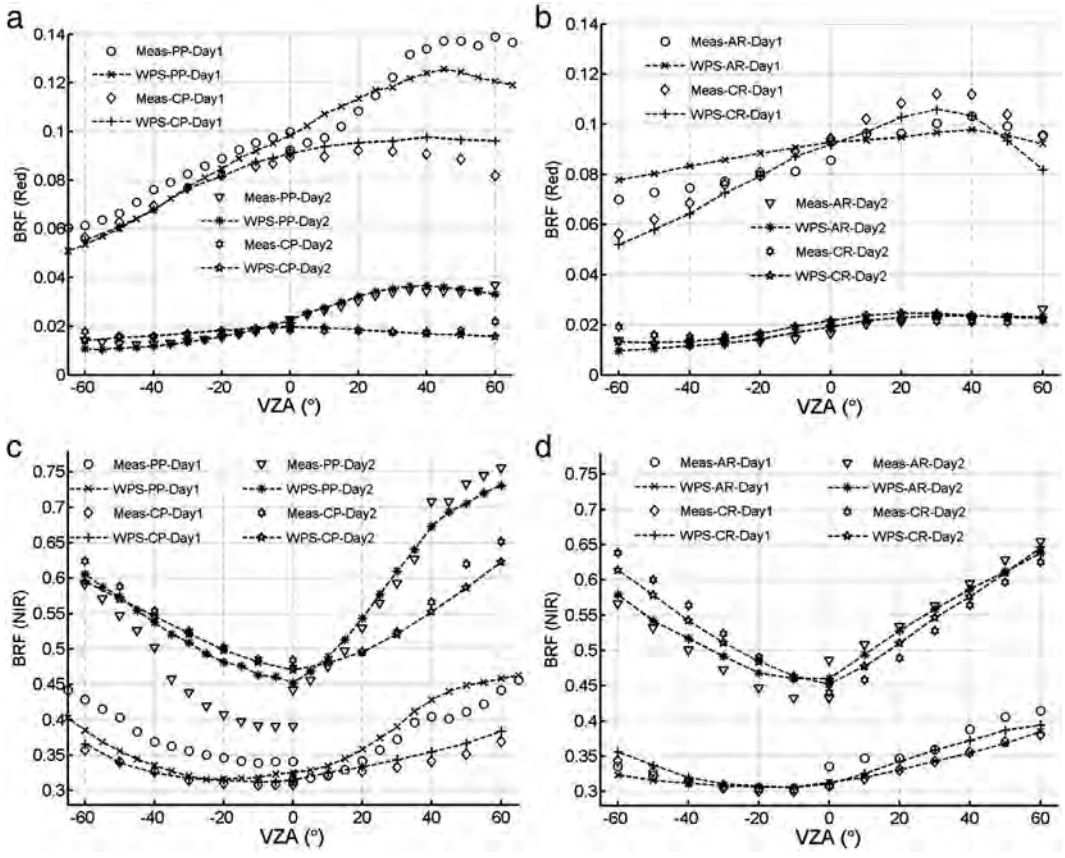

Fig. 3. The measured (noted as 'Meas-') and WPS simulated bidirectional reflectance factors (Day1 for Day-1, Day2 for Day-2) for different viewing zenith angles in red (a, b) and NIR (c, d) bands in four viewing azimuth planes: PP, CP, AR and CR.

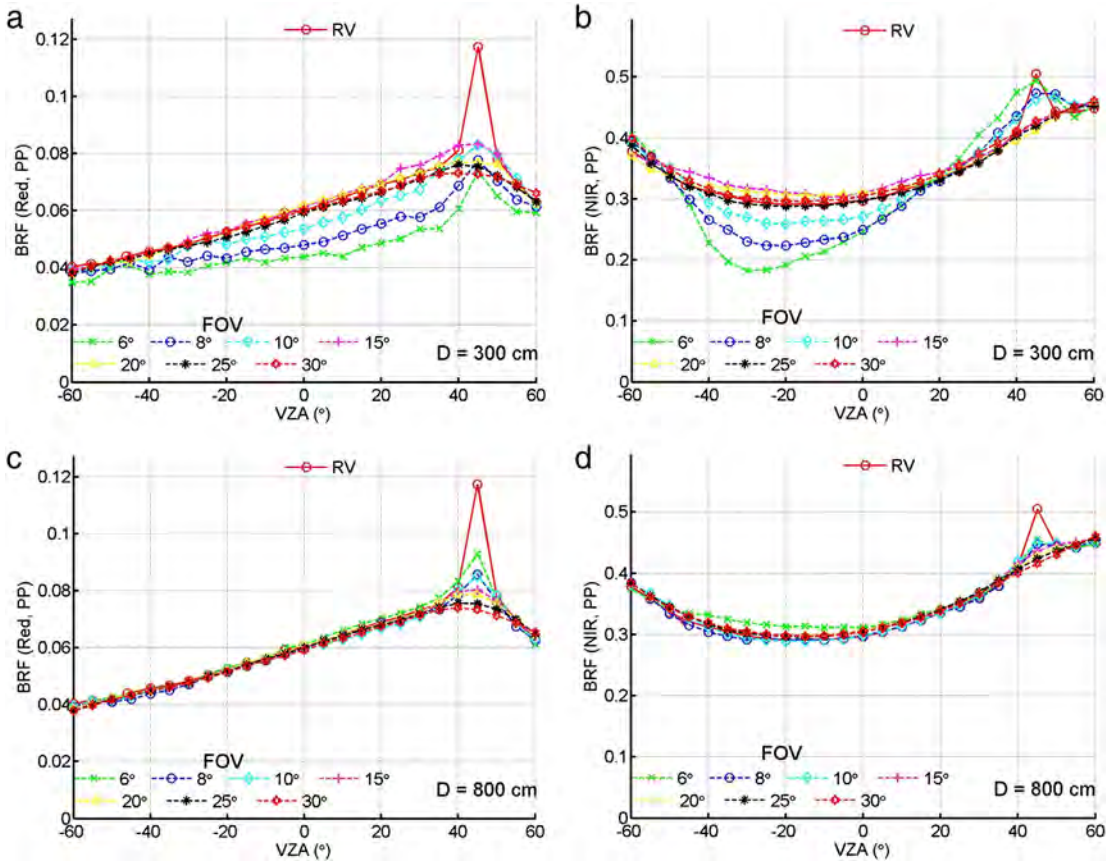

Fig. 4. Comparing examples of BRF distributions for different FOVs with the reference values (RVs) along PP in the red (a, c) and NIR (b, d) bands with the sensor located at 300 cm (a, b) and 800 cm (c, d) above the ground at nadir. The canopy scene is Row-1, illuminated by the sun in the direction of 45° (SZA) and 140° (SAA).

0.03 mrad (0.001739°) and the height to 560 km. This would provide a sampling distance of 17 m on ground at nadir for both along and cross track. With such a small FOV and long distance, we approximated the situation for a sensor located at infinity. The default perspective projection in POV-Ray was used to render the image with 600 pixels wide and 600 pixels high (i.e., a resolution of 600 × 600) for the ground level measurement, and resolution of 1600 × 1600 for space-borne device simulations. Such setting of the resolutions is high enough to adequately resolve the leaves on the output images.

4. Model application to study FOV and distance impact

4.1. Model evaluation

Comparison results of measured and simulated BRFs in red and NIR bands are shown in Fig. 3. The optical parameters of the canopy elements (leaf and soil) can be found in Table 2 of Zhao et al. (2010). Simulated BRFs agree fairly well with the measured ones, both in values and general shapes, though some differences are noticeable.

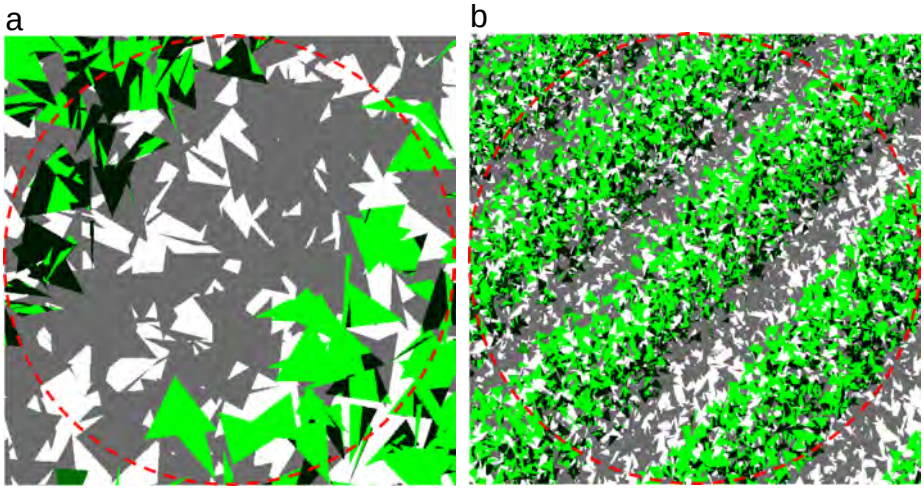

Fig. 5. Images rendered by POV-Ray for VZA of −30° in PP with sensor's FOV of 6° (a), and 30° (b) and distance of 300 cm for scene Row-1. Diameter of the circle is 31.44 cm (a) and 160.77 cm (b). The canopy is illuminated by the sun in the direction of 45° (SZA) and 140° (SAA). (For interpretation of the references to color in this figure, the reader is referred to the web version of this article.)

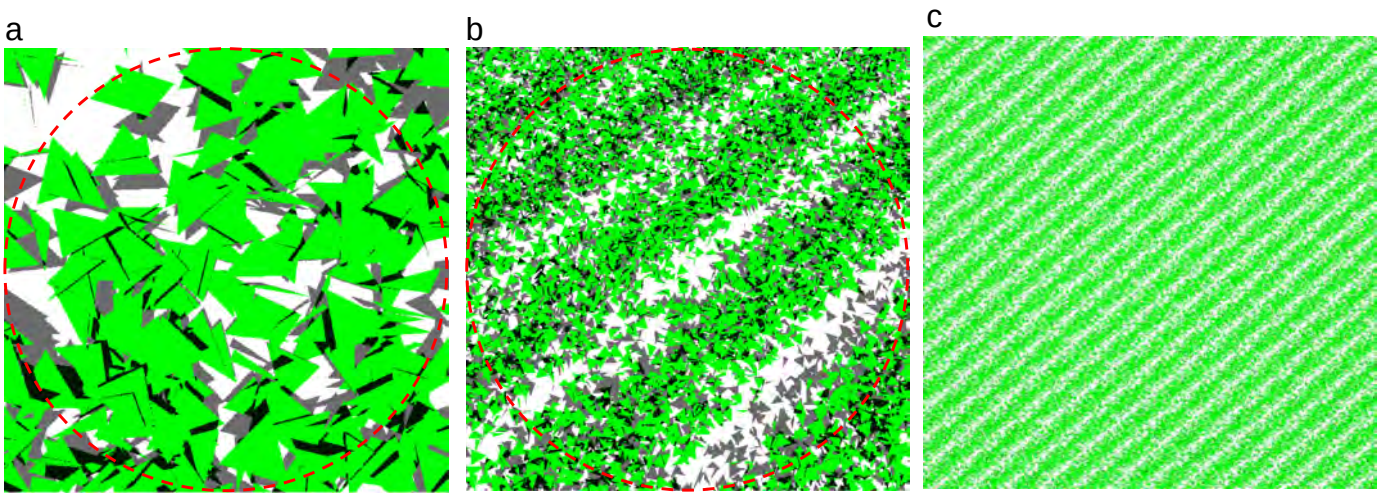

Fig. 6. Images rendered by POV-Ray for VZA of 45° in PP (hotspot direction) with the FOV of 6° (a), and 30° (b) and the distance of 300 cm for scene Row-1. Diameter of the circle is 31.44 cm (a) and 160.77 cm (b). For image c, the FOV and the height are 0.001739° and 560 km, respectively. SZA and SAA are 45°, and 140°, respectively. (For interpretation of the references to color in this figure, the reader is referred to the web version of this article.)

Besides the unstable weather conditions and heterogeneity in the wheat field (Zhao et al., 2010), one major source of the discrepancies is in the inaccuracies of the representation of the canopy. Due to lack of detailed 3-D arrangement data of the canopy elements, the scenes were generated by fitting their derived LAI, leaf inclination distributions and vegetation cover to the measured values and pictures. Leaves were represented by isosceles triangles and randomly distributed within the hedgerows. Therefore, the clumping effects within the row, the heterogeneity of the scene, and stems in the canopy were ignored, which may induce the inconsistency of canopy representation. Compared with the fitting results established between the measured BRFs and those simulated by the Row model, correlation coefficients between measured and simulated by WPS improve from 0.788 to 0.941 for red band, and 0.562 to 0.864 for NIR band, for Day-1. To a less degree for Day-2, they improve from 0.928 to 0.963, and 0.898 to 0.955 for red and NIR bands, respectively. Correspondingly, the root mean square errors reduce from 0.014 to 0.007 for red band, and 0.046 to 0.02 for NIR band, for Day-1, and 0.005 to 0.002 for red band, 0.04 to 0.031 for NIR band, for Day-2. The most evident improvements are found around the hotspot directions in PP (Fig. 3a, c). Without considering the finite FOV and distance of the sensor, row model produces a prominent hotspot (peak reflectance in the retro-illumination direction), which is mainly determined by the relative size of the leaves and the geometric structures of the row canopy. But for actual measurements, different VZAs mix within the FOV for the nominal VZA so as to smooth the BRF, especially for the region around the hotspot direction. This broad surge of BRFs around the hotspot direction can be better simulated with WPS by taking into account sensor FOV and distance. The agreement at higher VZAs also improves, especially for Day-1, which can be explained by the identical footprints simulated by WPS and measured by the spectrometer. Another possible source of differences arises from the neglect of the anisotropy of the soil reflectance. However, this non-Lambertian scattering function could be implemented fairly easily if the suitable distribution function is available.

In the supplement data, we also demonstrated that WPS compares very favorably with other well-established 3-D computer simulation models via the ROMC, with BRFs in both red and NIR bands within 1% of the corresponding ROMC reference data set. In the next part, we will use this model as a computational laboratory to study the impact of sensor configurations on the field measurement of BRFs.

4.2. Examples of BRF distributions for different experiments

Due to limited space, we only present several typical comparisons (Fig. 4) of BRF distributions between those measured for the sensor at the distance of 300 cm and 800 cm, and the RV for the scene Row-1 with SZA and SAA being 45° and 140°, respectively in PP. For the sensor distance to the target of 300 cm, the closeness of the agreement between BRFs measured by the sensor and the RVs improves with the FOV increases (Fig. 4a–b). In the red band (Fig. 4a), most BRFs for the

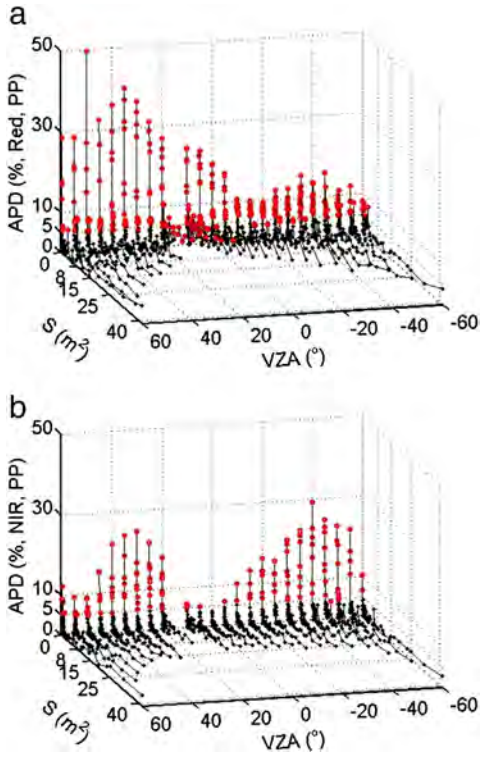

Fig. 7. Distributions of absolute percentage deviations (APDs) with the area of the footprint and VZAs in the red (a) and NIR (b) bands for scene Row-1 in PP. SZA and SAA are 15°, and 210°, respectively. APD with its value larger than 5% is marked with red color. (For interpretation of the references to color in this figure legend, the reader is referred to the web version of this article.)

sensor with the FOV of 6°, 8°, and 10° are systematically smaller than the RVs. And generally the wider the FOV is, the higher are the BRFs. This tendency holds for the NIR band (Fig. 4b) except around the hotspot directions, where BRFs by 6° FOV are larger than their counterparts with the FOV of 8° and 10°. In these directions, BRFs for the FOV of 6°, 8°, and 10° show the hotspot effect. But they are smaller than the RVs in the red band and larger than the RVs except for the hotspot direction (45°) in the NIR band. BRFs for the FOV of 15°, 20°, 25°, and 30° agree closely with the RVs for both the red and NIR bands. And almost the larger the FOV is, the better is the agreement. Though as close as they are, only a very broad and smooth hotspot effect appears in the red band compared with that of the RVs, and the effect is very weak or nearly absent in the NIR band.

When increased to a distance of 800 cm from the sensor to the center of the canopy (Fig. 4c–d), the agreements between BRFs by most FOVs and the RVs improve, especially for narrower FOVs, e.g. 6°, 8°, and 10°. The obvious deviations occur at VZAs around the hotspot direction for both bands, which go up with the FOV increases. To explain the distributions of BRFs for different sensor FOV–distance combinations as shown in Fig. 4, images rendered by POV-Ray under calibrated settings of geometric and sensor parameters between POV-Ray and WPS, are provided for selected viewing directions.

For a VZA of −30°, the BRF in the NIR band for all FOVs at the sensor distance of 300 cm is the smallest, significantly deviating from the RV (Fig. 4b). We then provided the image rendered by POV-Ray as shown in Fig. 5a, in which a red circle delineates the region contained in the footprint of the corresponding sensor (with FOV of 6° and distance of 300 cm). (Note that the POV-Ray rendered image is projected to the plane perpendicular to the primary axis. With the resolution of 600 × 600, the image has a square shape. For a sensor of given solid angle, the part in the maximum circle inside the square could be seen.) The green, black, white, and gray colors correspond to illuminated leaves, shaded leaves, illuminated soil, and shaded soil, respectively. A comparison image for the sensor with a FOV of 30° at the same distance is shown in Fig. 5b. From these figures, we can clearly see that only part of a single row can be 'seen' by the sensor with the FOV of 6° and the distance of 300 cm. In addition, this part is largely composed of shaded soil, which results in the smallest value of BRF in the NIR band. As a comparison, almost three rows appear in the sensor at the same distance with the FOV of 30° (Fig. 5b). The corresponding BRF for this VZA agrees closely with the RV (Fig. 4b), which indicates that a representative sample of the canopy is contained in the footprint of the measuring sensor.

Another distinct deviation occurs at the hotspot direction for all sensor configurations (Fig. 4). We selected the sensors positioned 300 cm away from the center of scene Row-1 with a FOV of 6° and 30°, and presented their corresponding rendered images for the hotspot direction as shown in Fig. 6. Trying to approximate the situation for a sensor located at infinity, we set the FOV to 0.03 mrad (0.001739°) and the sensor height at 560 km above the ground to render the image by POV-Ray, as shown in Fig. 6c. For finite FOV, only the center of the image corresponds to the exact hotspot direction with the sunlit elements. From the center outward, the points correspond to other different viewing zenith and azimuth angles where shaded components appear, which is quite evident in Fig. 6a–b. So, the mixture of different viewing angles

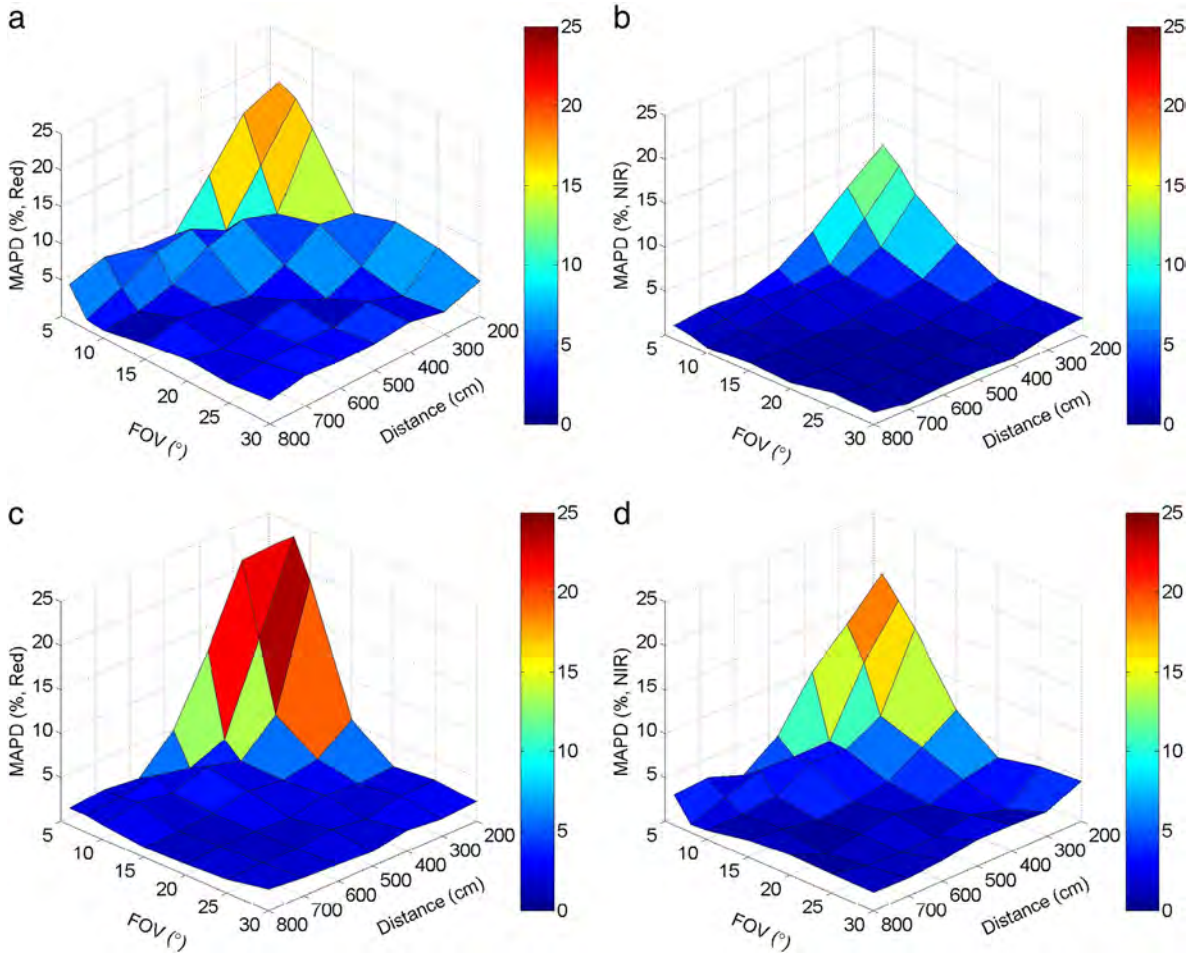

Fig. 8. Distributions of mean absolute percentage deviations (MAPDs) with the sensor FOV and distance combinations in the red (a, c) and NIR (b, d) bands for scene Row-1. SZA and SAA are 15°, and 210° for (a, b) and 45°, and 140° for (c, d), respectively. (For interpretation of the references to color in this figure legend, the reader is referred to the web version of this article.)

for finite FOV averages the within-pixel anisotropy and smoothes out the hotspot effect of BRF, especially for wider FOVs.

The much higher proportion of illuminated leaves for Fig. 6a results from the fact that only part of a single row is contained in the FOV of the sensor. Similar phenomena occur for adjacent viewing angles around the hotspot direction (not shown), which results in higher BRFs than the RVs for VZAs from 25° to 50° except for the hotspot direction in the NIR band (Fig. 4b). This feature does not appear in the red band (Fig. 4a) because of the much lower reflectance and transmittance of the leaf. Though more than three rows appear in the sensor at the same sensor distance with the FOV of 30° (Fig. 6b), the high fractions of the shaded components, totaling to around 0.3, significantly weaken the hotspot effect in both bands.

Although only limited comparison results of BRF distributions in PP for specific sensor FOV–distance combinations for scene Row-1 with their RVs were presented, a general trend as shown here also manifested for the two row scenes, both red and NIR bands, different sun angles (Table 4) and viewing planes: the deviations decrease with the increase of sensor's FOV or distance, or both of them, especially when the deviations result from the non-representative samples of the canopy detected by the sensor. Though viewing angles mix across the FOV of the sensor for a nominal viewing direction during in situ BRDF measurements, BRFs could agree quite closely with their corresponding RVs, except for the hotspot direction and the directions around it when a representative sample is enclosed in the FOV of the sensor. The reason lies mainly in the fact that the distributions of BRF for regularly spaced row canopy are smooth, except in the hotspot direction (Zhao et al., 2010). Therefore, the decrement of the radiative contribution is always compensated by the increment within the FOV, or vice versa. This gradual stabilization of field directional reflectance measurement is consistent with the phenomenon of stationarity in cloud physics, which means that reasonably accurate estimates of climatological averages can be obtained by using reasonable amounts of data during spatial scaling of observation (Davis, Marshak, Wiscombe, & Cahalan, 1996). Widlowski, Pinty, et al. (2006) studied the stationarity issue of simulated 3-D coniferous forest, and found the manifestation of structural (LAI, tree density and tree height) and radiative (albedo) stationarity when observed by sensors with medium spatial resolution (ranging from ≈250 m to 1.5 km). Here we revealed the similar stationary behavior of BRF in the field experiment for row canopies.

Around the hotspot directions, generally a global maximum for the visible bands and a local maximum for the NIR bands exist, and the slowly varying distributions of BRFs do not hold. Therefore, the lower BRFs around the hotspot directions bring down the peak of the hotspot by the averaging process, resulting in a weak hotspot effect or even the absence of it, whose extent depends on the sensor FOV, the width of the hotspot, and the spectral band. In the next part, we will explore the variance of the deviations from the RVs as a function of sensor FOV–distance combinations with more statistical results.

4.3. Variance of the deviations versus sensor FOV and distance

The portion of row canopy in the sensor's FOV changes with the FOV and the distance of the sensor, and regulates the extent of the deviations from the RV. By employing the semidiameter of the circular footprint, major and minor semiaxes of the elliptical footprint (Eq. 7) for different measuring sensors, we analyzed the variance of the deviations from the RV. First, we present the distributions of the absolute percentage deviation (APD) in the PP.

4.3.1. The absolute percentage deviations in the principal plane

APDs in both the red and NIR bands for scene Row-1 were plotted in Fig. 7 with the areas (S) of the elliptic (or circular) footprint for different sensor FOV and distance combinations under different VZAs in PP with SZA and SAA of 15° and 210°, respectively. Distributions of APD for Row-1 in PP with SZA of 45° and SAA of 140° are similar and not shown here. Since all the sensors at the ground level (Table 3) are not capable of effectively capturing the hotspot effect, APDs in the hotspot direction (VZA = 15°) were not included in the figures. BRFs by which their APDs are less than 5% with respect to the RVs are considered to be tolerable, in accordance with the 3–5% error margins obtained by vicarious calibration of space-borne remote sensing devices in the visible and NIR bands (e.g. Wang et al., 2011; Widlowski et al., 2013). APD with its value larger than 5% is marked with red color. For most VZAs, APDs in both bands decrease rapidly to the tolerance criterion (5%) with the increase of the areas of the elliptic footprint, which results from the increase of sensor's FOV or/and distance. The increase of the area does not necessarily lead to the further decrease of APD, though mostly they are still smaller than the tolerance criterion. For both solar positions, APDs in the NIR band (Fig. 7b) generally decrease faster with the increase of the areas, and relatively keep more stable when APDs are smaller than the tolerance criterion, compared with APDs in the red band (Fig. 7a). The inspection of the APD distributions for the single and multiple scattering contributions in the NIR band (not shown) reveals that APDs for the multiple scattering contributions are generally smaller than those for the single scattering contributions, which are similar to APDs in the red band. This is reasonable considering the relatively isotropic nature of multiple scattering contributions. Since both single and multiple scattering contributions in the NIR band play important roles for the total BRF of the row canopies (Zhao et al., 2010), the resulting APDs show differences

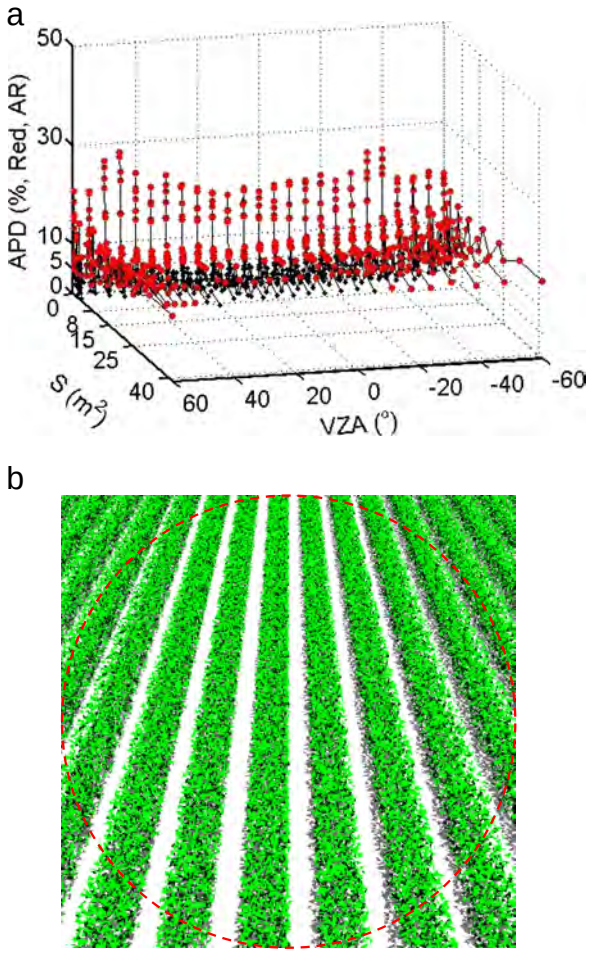

Fig. 9. Distributions of absolute percentage deviations (APDs) with the area of the footprint and VZAs in the red (a) band for scene Row-1 in AR, and the image rendered by POV-Ray for VZA of 60° in AR with the FOV of 30° and the distance of 800 cm for scene Row-1 (b). Diameter of the circle is 428.72 cm (b). SZA and SAA are 15°, and 210° respectively. APD with its value larger than 5% is marked with red color. (For interpretation of the references to color in this figure legend, the reader is referred to the web version of this article.)

in the red and NIR bands. This phenomenon is similar to the smoothing effect of radiative transfer, or "radiative smoothing", e.g., Marshak, Davis, Wiscombe, and Cahalan (1995) and Widlowski, Pinty, et al. (2006).

Similar patterns of APD distributions in PPs appear for scene Row-2 (not shown). Compared with APDs for Row-1, generally lower magnitudes are observed, probably because of higher LAI (2.2 for Row-2 and 1.3 for Row-1) with similar canopy cover (around 0.6).

4.3.2. Distributions of mean absolute percentage deviations of four viewing planes

By averaging all APDs of BRF for VZA from −60° to 60° with a step of 5° in four planes under the same solar position excluding the hotspot direction, we obtained the distributions of mean absolute percentage deviations (MAPDs) with respect to sensor FOV and distance in both the red and NIR bands for scene Row-1 as illustrated in Fig. 8. The general trends shown in Fig. 8 are consistent with those for APDs in PP (Fig. 7). MAPDs in both bands decrease with the increase of the sensor FOV and distance. Although the extents of the decrease are different in the red and NIR band, and for different solar positions, the tolerance criterion of 5% for MAPD can be reached, as early as for the combinations of intermediate FOV and distance values. The difference for the distributions of MAPDs appears with regard to the spectral bands. Under the same solar position, the magnitudes of MAPDs in the NIR band are generally smaller than those in the red band and the distribution of MAPDs is much smoother in the NIR band due to radiative smoothing. Different from all other distributions of MAPDs, there are some fluctuations for MAPDs in the red band for SZA of 15° and SAA of 210° (Fig. 8a). By close inspection of the distributions of APDs in all four planes, we found that the fluctuations arose from the AR plane.

APDs in the red band for scene Row-1 in AR with SZA and SAA of 15° and 210°, respectively, are shown in Fig. 9, together with an image with VZA of −60° rendered by POV-Ray. Unlike other three viewing planes (PP, CP and CR), in which the distribution of APDs in the red band is similar to that in Fig. 7a, APDs in AR (Fig. 9a) fluctuate continuously after the initial rapid decrease with the increase of the area of the elliptic footprint. The fluctuations are more evident for high VZAs, for example ±60°, where most APDs are larger than 5%. Rendered images for VZA of −60° was shown in Fig. 9b, with the sensor of a 30° FOV located at a distance of 800 cm to the center of the scene. The characteristic feature of perspective projection is evident for the high VZA (−60°) in AR in the image: objects are smaller as their distance from the sensor increases. Therefore, more rows further away are included in the upper part of the image, which induces distortions of components' proportions. The comparison of four components' fractions between this image and that acquired by a space-borne device reveals that sunlit soil is underestimated with a relative difference of 18%, and shaded soil, sunlit leaves, and shaded leaves are all overestimated by 20%, 8%, and 13%, respectively. As a comparison with the same sensor observing in PP except for the hotspot direction, the relative difference of four components' fractions is in the range of ±10%, and that of sunlit soil and leaves is in the range of ±5%. The solar position with small zenith angle (15°) and close to the row orientation (210°) for relatively clear row structure, combined with the evident distortion of perspective projection in this viewing direction (−60° in AR), results in the large difference of

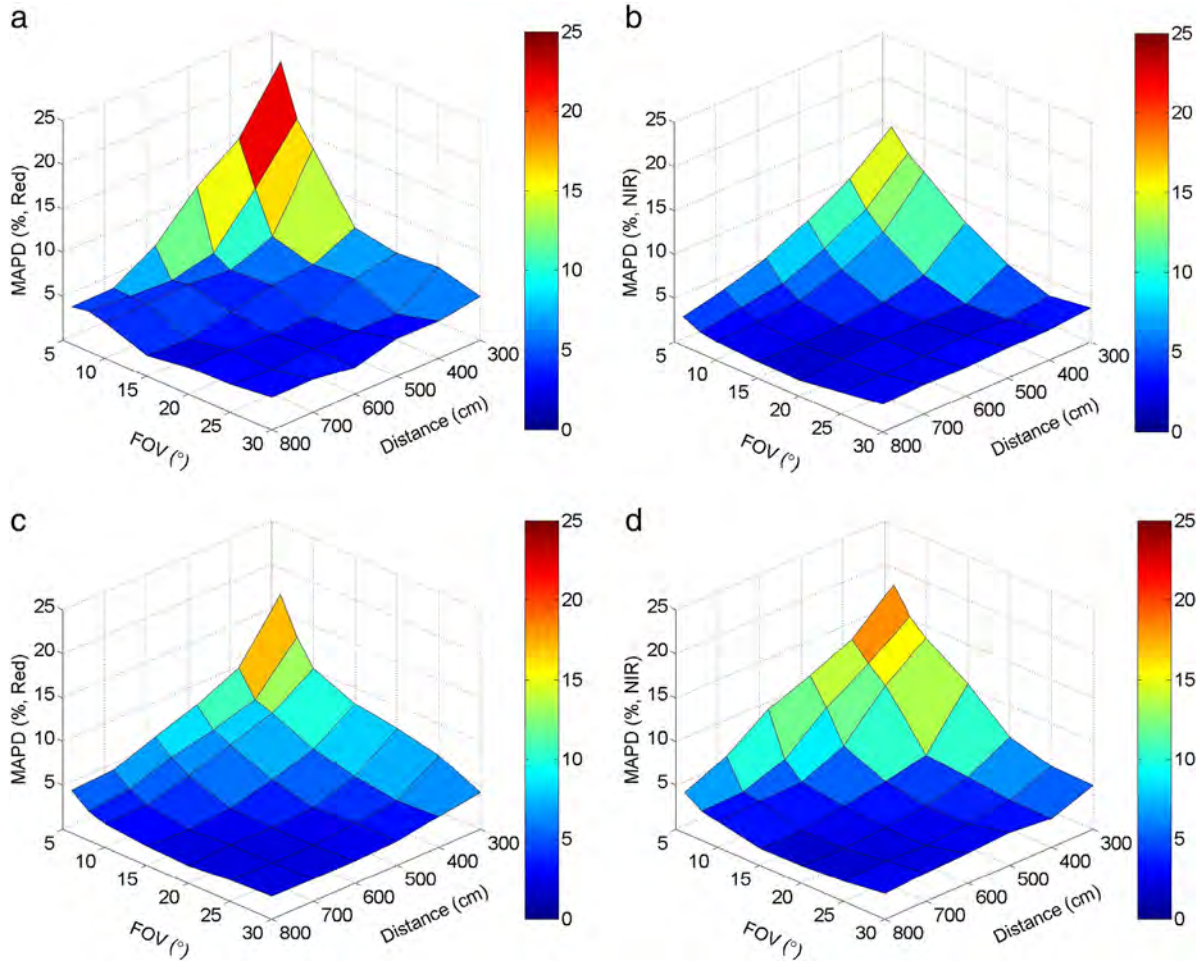

Fig. 10. Distributions of mean absolute percentage deviations (MAPDs) with the sensor FOV and distance combinations in the red (a, c) and NIR (b, d) bands for scene Row-2. SZA and SAA are 25°, and 220° for (a, b) and 46°, and 105° for (c, d), respectively. (For interpretation of the references to color in this figure legend, the reader is referred to the web version of this article.)

the fractions. Therefore, the high deviation from the RV appears at this VZA. Similar reasons apply for other VZAs in AR, and lead to the fluctuations in Fig. 9a and finally Fig. 8a. Since APDs in other viewing planes decrease rapidly with the increase of the area of the elliptic footprint, MAPD still can reach the tolerance criterion and keep low values after that. But care should be taken when carrying out BRF measurements in visible bands in AR for high solar position and sparse row canopies. Because the significant radiative smoothing effect in the NIR band, the evident fluctuations are absent. For the solar position of low angles, e.g. SZA of 45° and SAA of 140°, the deviation of the sunlit components' fractions is much smaller (in the range of ±7%). So no similar fluctuations appear in Fig. 8c for MAPDs in the red band.

Fig. 10 shows the distributions of MAPDs with respect to sensor FOV and distance in both the red and NIR bands for scene Row-2. MAPDs in both spectral bands decrease smoothly with the increase of sensor FOV and distance. Though the distribution of MAPDs in the red band for SZA of 25° and SAA of 220° (Fig. 10a) is not so regular compared with the other three figures, it is much less fluctuating than the one in Fig. 8a.

To further investigate the influence of the size of the footprint of the sensor on MAPDs, we calculated the diameters of the circular footprint on the ground at nadir for different sensor FOV and distance combinations. The larger one of the MAPDs in red and NIR bands for the same solar position and sensor combination is chosen and plotted against the diameter in Fig. 11. It is shown that MAPDs for those diameters smaller than the row spacing (50 cm for Row-1 and 70 cm for Row-2) are large (mostly larger than 5%). This is reasonable because only a portion of the row canopy can be seen by the sensor. With the increase of the diameter, MAPDs generally decrease, though the extents are different for different solar positions. For MAPDs less than 5%, there are some local maximums, which mostly correspond to large FOVs, e.g. 25° and 30°.

By inspecting the MAPDs less than 5% and their corresponding diameters (at nadir), we can find three groups of diameters, and each with three or four close diameter values (less than 5% among them). The diameters of the three groups are around 105 cm, 177 cm and 211 cm, noted as D1, D2, and D3, respectively. MAPDs for the close diameters of each group are plotted into lines for Row-1 (Fig. 12a) and Row-2 (Fig. 12b), under the same solar position and in the same spectral band. Most MAPDs for the same group for Row-1 (Fig. 12a) and all of them for Row-2 (Fig. 12b) show the same tendency: they increase with the increase of sensor FOV. So under the condition that the BRF sampling stationarity is reached, the sensor with narrower FOV (correspondingly with larger distance) should be preferred to reduce the bias in the BRF measurements. This is reasonable, considering the stronger averaging process for the wider FOV of the sensor around the nominal viewing direction.

5. Conclusions

The reflectance anisotropy is one of the characteristic properties of natural surfaces. Spectral measurements of the directional reflectance at ground level provide us a method to capture the directional reflectance characteristics of the observed surface. Because of the uncontrollable environmental influences on acquiring costly ground spectral BRF data, simulated data by a MC model were used to study the impact of sensor FOV and distance on field measurement of BRFs.

Due to the substantial amount of processing time required for a traditional MC model, a variance reduction method of photon spread with a weight reduction concept was adopted to develop a new computer simulation model, namely the weighted photon spread (WPS) model. Comparisons with field BRF measurements as well as comparisons via

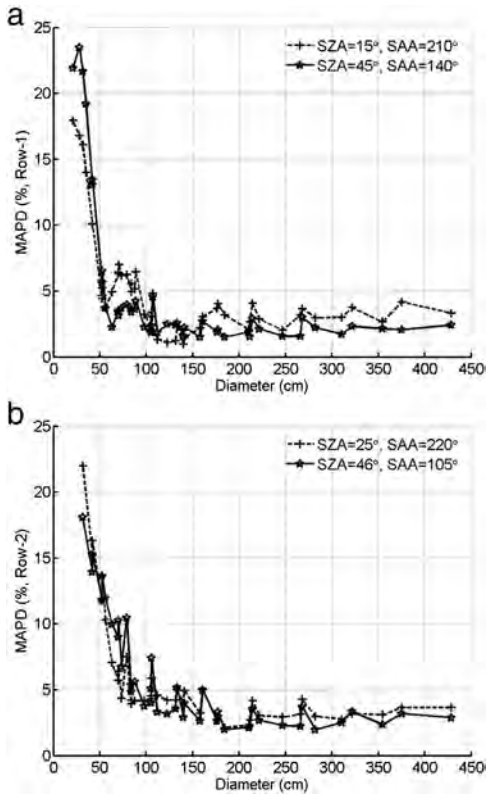

Fig. 11. Distributions of mean absolute percentage deviations (MAPDs) with the diameters of the circular footprint on the ground at nadir for different sensor FOV and distance combinations for Row-1 (a) and Row-2 (b). Under the same solar position and sensor combination, MAPD is the larger one in the red and NIR bands.

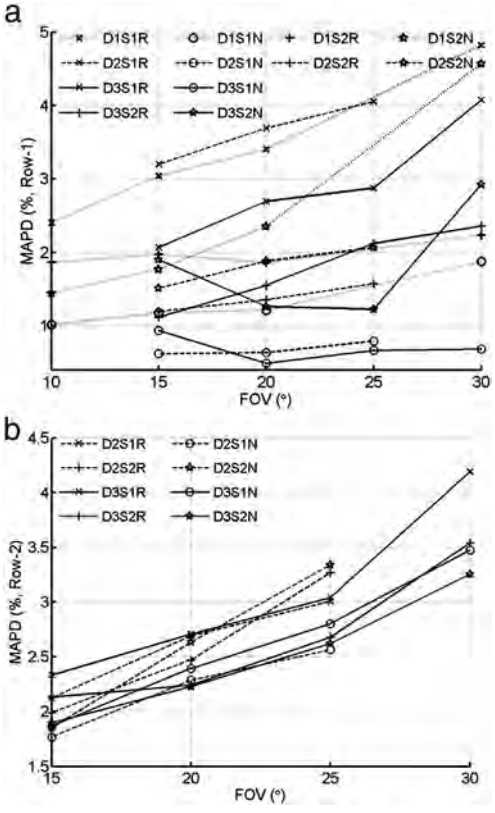

Fig. 12. Variance of mean absolute percentage deviations (MAPDs) for close diameter values of the footprint with sensor FOV for Row-1 (a) and Row-2 (b). D1 stands for 105 cm, D2 for 177 cm and D3 for 211 cm. For Row-1 (a), SZA, and SAA for 'S1' and 'S2' correspond to (15°, 210°) and (45°, 140°) respectively. For Row-2 (b), SZA, and SAA for 'S1' and 'S2' correspond to (25°, 220°) and (46°, 105°) respectively. 'R' stands for the red band, and 'N' for the NIR band.

RAMI Online Model Checker (ROMC) show that WPS is capable of faithfully reproducing the angular distribution of the canopy BRFs.

The BRFs simulated for a range of sensor FOV and distance combinations were compared with the reference values for two typical row canopy scenes. Sensors with a finite FOV and distance to the target approximate the true BRFs and yield average values over FOV. Moreover, the perspective projection of the sensor causes the proportional distortion in the sensor FOV from the ideal directional observations. Though such factors inducing the measurement error exist, it was found that BRF can be sampled with a tolerable bias on the ground level with proper combinations of sensor FOV and distance except for the hotspot direction and the directions around it. This is so because of the generally smooth distributions of the BRF for regularly spaced row canopies except for the hotspot direction. The proper combination of sensor FOV and distance ensures that a representative sample of the canopy is included in the FOV of the sensor, and consequently the stationarity of BRF sampling is reached. But the onset of this stationarity changes with row structure, solar position, viewing plane and angles, spectral band, and sensor FOV and distance combination. Generally, longer distances of the sensor from the target and wider FOVs are recommended under permitted conditions. And the former is preferred over the latter, because a wider FOV enhances the averaging effect within the FOV, resulting in higher deviations from the real angular signatures. Besides, we suggest to use a computer simulation model (e.g. WPS) before the field measurement to guide the choice of the device and the design of the measurement protocols.

Acknowledgments

This work was supported by the Chinese Natural Science Foundation (Projects 41371325 and 40901156), and the Project of Civil Space Technology pre-research of the 12th five-year plan (D040201). We thank POV-Ray team for providing their software. Dr. Feng Zhao would like to thank Dr. Jean-Luc Widlowski for his helpful suggestions and comments on this work during the 35th International Symposium on Remote Sensing of Environment (Beijing, 23th–26th April, 2013). We are thankful to the ROMC coordinators during the model evaluation. The authors are also grateful to the anonymous reviewers who provided constructive comments to improve this manuscript.

Appendix A. Supplementary data

Supplementary data to this article can be found online at http://dx.doi.org/10.1016/j.rse.2014.09.011.

References

Abdou, W. A., Helmlinger, M. C., Conel, J. E., Bruegge, C. J., Pilorz, S. H., Martonchik, J. V., et al. (2001). Ground measurements of surface BRF and HBRF using PARABOLA III. *Journal of Geophysical Research*, *106*, 11967–11976.

Anderson, K., Rossini, M., Pacheco-Labrador, J., Balzarolo, M., Mac Arthur, A., Fava, F., et al. (2013). Inter-comparison of hemispherical conical reflectance factors (HCRF) measured with four fibre-based spectrometers. *Optics Express*, *21*, 605–617.

Antyufeev, V. S., & Marshak, A. L. (1990). Monte Carlo method and transport equation in plant canopies. *Remote Sensing of Environment*, *31*, 183–191.

Buchhorn, M., Petereit, R., & Heim, B. (2013). A manual transportable instrument platform for ground-based spectro-directional observations (ManTIS) and the resultant hyperspectral field goniometer system. *Sensors*, *13*, 16105–16128.

Cutter, M.A. (2004). Compact high-resolution imaging spectrometer (CHRIS) design and performance. *Optical Science and Technology, the SPIE 49th Annual Meeting* (pp. 126–131).

Daughtry, C., Vanderbilt, V., & Pollara, V. (1982). Variability of reflectance measurements with sensor altitude and canopy type. *Agronomy Journal*, *74*, 744–751.

Davis, A. B., Marshak, A., Wiscombe, W. J., & Cahalan, R. F. (1996). Scale invariance in liquid water distributions in marine stratocumulus. Part I: Spectral properties and stationarity issues. *Journal of the Atmospheric Sciences*, *53*, 1538–1558.

Deering, D. W., & Eck, T. F. (1987). Atmospheric optical depth effects on angular anisotropy of plant canopy reflectance. *International Journal of Remote Sensing*, *8*, 893–916.

Deering, D. W., Eck, T. F., & Grier, T. (1992). Shinnery oak bidirectional reflectance properties and canopy model inversion. *IEEE Transactions on Geoscience and Remote Sensing*, *30*, 339–348.

Deering, D. W., & Leone, P. (1986). A sphere-scanning radiometer for rapid directional measurements of sky and ground radiance. *Remote Sensing of Environment*, *19*, 1–24.

Eck, T. F., & Deering, D. W. (1992). Spectral bidirectional and hemispherical reflectance characteristics of selected sites in the Streletskaya steppe. *Geoscience and Remote Sensing Symposium. 1992. IGARSS'92. International*, *2*. (pp. 1053–1055).

El-Shikha, D., Waller, P., Hunsaker, D., Clarke, T., & Barnes, E. (2007). Ground-based remote sensing for assessing water and nitrogen status of broccoli. *Agricultural Water Management*, *92*, 183–193.

Gamon, J. A., Cheng, Y., Claudio, H., MacKinney, L., & Sims, D. A. (2006). A mobile tram system for systematic sampling of ecosystem optical properties. *Remote Sensing of Environment*, *103*, 246–254.

Gianelle, D., & Guastella, F. (2007). Nadir and off-nadir hyperspectral field data: strengths and limitations in estimating grassland biophysical characteristics. *International Journal of Remote Sensing*, *28*, 1547–1560.

Giardino, C., & Brivio, P. (2003). The application of a dedicated device to acquire bidirectional reflectance factors over natural surfaces. *International Journal of Remote Sensing*, *24*, 2989–2995.

Goel, N. S. (1988). Models of vegetation canopy reflectance and their use in estimation of biophysical parameters from reflectance data. *Remote Sensing Reviews*, *4*(1), 1–212.

Govaerts, Y. M. (1996). *A model of light scattering in three-dimensional plant canopies: A Monte Carlo ray tracing approach.* (Ph.D. Thesis). JRC catalogue no. CL-NA-16394-ENC. Luxembourg: Office for Official Publications of the European Communities.

Govaerts, Y. M., & Verstraete, M. M. (1998). Raytran: A Monte Carlo ray-tracing model to compute light scattering in three-dimensional heterogeneous media. *IEEE Transactions on Geoscience and Remote Sensing*, *36*, 493–505.

Huang, X., Jiao, Z., Dong, Y., Zhang, H., & Li, X. (2013). Analysis of BRDF and Albedo Retrieved by Kernel-Driven Models Using Field Measurements. *IEEE Journal of Selected Topics in Applied Earth Observations and Remote Sensing*, *6*(1), 149–161.

Iwabuchi, H. (2006). Efficient Monte Carlo methods for radiative transfer modeling. *Journal of the Atmospheric Sciences*, *63*, 2324–2339.

Kimes, D. (1983). Dynamics of directional reflectance factor distributions for vegetation canopies. *Applied Optics*, *22*, 1364–1372.

Kimes, D. S., Newcomb, W. W., Tucker, C. J., Zonneveld, I. S., Van Wijngaarden, W., De Leeuw, J., et al. (1985). Directional reflectance factor distributions for cover types of Northern Africa. *Remote Sensing of Environment*, *18*, 1–19.

Mac Arthur, A., MacLellan, C. J., & Malthus, T. (2012). The fields of view and directional response functions of two field spectroradiometers. *IEEE Transactions on Geoscience and Remote Sensing*, *50*, 3892–3907.

Marshak, A. L., Davis, A. B., Wiscombe, W. J., & Cahalan, R. F. (1995). Radiative smoothing in fractal clouds. *Journal of Geophysical Research*, *100*, 26,247–26,261.

Milton, E. J. (1987, Dec.). Principles of field spectroscopy. *International Journal of Remote Sensing*, *8*, 1807–1827.

Milton, E. J., Schaepman, M., Anderson, K., Kneubühler, M., & Fox, N. (2009, Sep.). Progress in field spectroscopy. *Remote Sensing of Environment*, *113*(Suppl. 1), S92–S109.

Nicodemus, F. F., Richmond, J. C., Hsia, J. J., Ginsberg, I. W., & Limperis, T. L. (1977). *Geometrical considerations and nomenclature for reflectance. National Bureau of Standards Monograph, Vol. 160*, Washington D.C.: U.S. Govt. Printing Office.

Pinter, P. J., Jr., Jackson, R. D., & Moran, M. S. (1990). Bidirectional reflectance factors of agricultural targets: A comparison of ground-, aircraft-, and satellite-based observations. *Remote Sensing of Environment*, *32*, 215–228.

POV-team (2009). Introduction to POV-Ray for POV-Ray version 3.62. http://www.povray.org

Ranson, K., Irons, J., & Daughtry, C. (1991). Surface albedo from bidirectional reflectance. *Remote Sensing of Environment*, *35*, 201–211.

Ren, H., Yan, G., Liu, R., Nerry, F., Li, Z. L., & Hu, R. (2013). Impact of sensor footprint on measurement of directional brightness temperature of row crop canopies. *Remote Sensing of Environment*, *134*, 135–151.

Ross, J. K., & Marshak, A. (1988). Calculation of canopy bidirectional reflectance using the Monte Carlo method. *Remote Sensing of Environment*, *24*, 213–225.

Sandmeier, S. R., & Itten, K. I. (1999). A field goniometer system (FIGOS) for acquisition of hyperspectral BRDF data. *IEEE Transactions on Geoscience and Remote Sensing*, *37*, 978–986.

Schaepman-Strub, G., Schaepman, M. E., Painter, T. H., Dangel, S., & Martonchik, J. V. (2006). Reflectance quantities in optical remote sensing—Definitions and case studies. *Remote Sensing of Environment*, *103*, 27.42.

Secker, J., Staenz, K., Gauthier, R. P., & Budkewitsch, P. (2001). Vicarious calibration of airborne hyperspectral sensors in operational environments. *Remote Sensing of Environment*, *76*, 81–92.

Shang, H., Zhao, F., & Zhao, H. (2012). The analysis of errors for field experiment based on POV-Ray. *Geoscience and Remote Sensing Symposium. 2012, IGARSS 2012, Munich, Germany* (pp. 4805–4808).

Strahler, A. H. (1997). Vegetation canopy reflectance — Recent developments and remote sensing perspectives. *Remote Sensing Reviews*, *15*, 179–194.

Strub, G., Schaepman, M., Knyazikhin, Y., & Itten, K. I. (2003). Evaluation of spectrodirectional Alfalfa canopy data acquired during DAISEX'99. *IEEE Transactions on Geoscience and Remote Sensing*, *41*, 1034.1042.

Thompson, R. L., & Goel, N. S. (1998). Two models for rapidly calculating bidirectional reflectance of complex vegetation scenes: Photon spread (PS) model and statistical photon spread (SPS) model. *Remote Sensing Reviews*, *16*, 157–207.

Vierling, L. A., Deering, D. W., & Eck, T. F. (1997). Differences in arctic tundra vegetation type and phenology as seen using bidirectional radiometry in the early growing season. *Remote Sensing of Environment*, *60*, 71–82.

Walthall, C., Roujean, J. L., & Morisette, J. (2000). Field and landscape BRDF optical wavelength measurements: Experience, techniques and the future. *Remote Sensing Reviews*, *18*, 503–531.

Wang, Y., Czapla-Myers, J., Lyapustin, A., Thome, K., & Dutton, E. (2011). AERONET-based surface reflectance validation network (ASRVN) data evaluation: Case study for railroad valley calibration site. *Remote Sensing of Environment*, *115*, 2710–2717.

Wang, L., Jacques, S. L., & Zheng, L. (1995). MCML—Monte Carlo modeling of light transport in multi-layered tissues. *Computer Methods and Programs in Biomedicine*, *47*, 131–146.

Wang, J., Zhao, F., Li, H., Yu, T., Gu, X., Xue, L., et al. (2010). Sunlit components' fractions and gap fraction of canopies based on POV-Ray. *Journal of Remote Sensing*, *14*, 232–251.

Widlowski, J. L., Lavergne, T., Pinty, B., Verstraete, M., & Gobron, N. (2006). *Rayspread: A virtual laboratory for rapid BRF simulations over 3-D plant canopies.* Computational Methods in Transport. Springer, 211–231.

Widlowski, J. L., Pinty, B., Lavergne, T., Verstraete, M., & Gobron, N. (2006). Horizontal radiation transport in 3-D forest canopies at multiple spatial resolutions: Simulated impact on canopy absorption. *Remote Sensing of Environment*, *103*, 379–397.

Widlowski, J. -L., Robustelli, M., Disney, M., Gastellu-Etchegorry, J. -P., Lavergne, T., Lewis, P., et al. (2008). The RAMI On-line Model Checker (ROMC): A web-based benchmarking facility for canopy reflectance models. *Remote Sensing of Environment*, *112*(3), 1144–1150.

Widlowski, J. -L., Pinty, B., Lopatka, M., Atzberger, C., Buzica, D., Chelle, M., et al. (2013). The fourth radiation transfer model intercomparison (RAMI-IV): Proficiency testing of canopy reflectance models with ISO-13528. *Journal of Geophysical Research*, *118*, 1–22.

Zhao, F., Gu, X., Verhoef, W., Wang, Q., Yu, T., Liu, Q., et al. (2010). A spectral directional reflectance model of row crops. *Remote Sensing of Environment*, *114*(2), 265–285.

Zhao, F., Gu, X., Yu, T., Verhoef, W., Guo, Y., Du, Y., et al. (2013). Bidirectional reflectance effects over flat land surface from the charge-coupled device data sets of the HJ-1A and HJ-1B satellites. *Journal of Applied Remote Sensing*, *7* (073466-073466).